

INVESTIGATING ARTERIAL GEOMETRY RISK FACTORS FOR CAROTID ARTEROSCLEROTIC DISEASE

Matt D. SINNOTT^{1*}, Simon HARRISON¹, Thanh PHAN², Richard BEARE², Velandai SRIKANTH² and Paul W. CLEARY¹

¹ CSIRO Mathematics, Informatics and Statistics, Clayton, Victoria 3169, AUSTRALIA

² Stroke and Ageing Research Group, Monash Medical Centre, Monash University, Victoria 3800, AUSTRALIA

*Corresponding author, E-mail address: Matthew.Sinnott@csiro.au

ABSTRACT

The breadth in patient demographics exhibiting carotid artery disease is not explained by traditional vascular risk factors (such as smoking). A recent clinical study of a cross-section of high risk factor patients undergoing Computed Tomography (CT) angiography has linked aspects of carotid geometry, namely bifurcation angle and internal carotid artery (ICA) diameter, to the pathogenesis of ICA stenosis. Large ICA angle and small radius are implicated as potential risk factors. Abnormal wall shear stress has been found for ICA angles greater than 25°. These patient-specific factors together with traditional factors may aid the early identification of patients at high risk of developing carotid arterosclerosis requiring surgical intervention. Here, we test the hypothesis of that study using flow simulations in a real, clinical carotid geometry. The meshless method, Smoothed Particle Hydrodynamics, is used to simulate blood flow through the carotid bifurcation. We assume the flow to be Newtonian and pulsatile and the walls to be rigid. The resulting flow field and arterial wall shear stresses are investigated for a range of carotid geometry variants where the bifurcation angle is artificially modified from the original clinical model. Finally we investigate the interaction between time-varying flow and different outflow pressure boundary conditions and how these influence arterial flow and wall stresses.

NOMENCLATURE

A	Generic SPH function
m	mass
W	SPH smoothing kernel function
r	position
P	pressure
h	kernel support
v	velocity
t	time
g	gravity vector
ζ	viscous factor
η	correction factor for SPH momentum equation
γ	index for equation of state
ρ	density
μ	dynamic viscosity

INTRODUCTION

Carotid artery disease affects a broad patient demographic and the traditional set of risk factors used to assess patients for early surgical intervention are not sufficient. Additional patient-specific factors that relate to specific

mechanisms for disease (such as those relating to blood flow and wall stress) may aid the early identification of patients that are at high risk of cerebral stroke.

Recently, Phan et al. (2012) have shown clinical evidence using Computed Tomography (CT) angiography that aspects of carotid geometry may be related to the onset of vascular disease, although the underlying mechanisms are not yet identified. Specifically their findings suggested that patients with large bifurcation angle in their carotid arteries and with small internal carotid artery (ICA) radius appear more predisposed to developing arterosclerosis (arterial hardening). Nguyen et al. (2008) have identified abnormal wall shear stress (WSS) for patients with ICA angles larger than about 25°.

This study aims to understand flow-related mechanisms underpinning the predicted relationship between carotid artery disease and ICA angle from Phan et al. (2012). This involves taking a clinical patient geometry derived from CT, and artificially modifying the ICA angle to create a set of new geometries with different branch angles. We then investigate changes in flow and wall stress for different angles.

MODEL DESCRIPTION

Smoothed Particle Hydrodynamics

The flow simulations are performed using the CSIRO Smoothed Particle Hydrodynamics (SPH) solver (see Cleary et al., 2007). SPH is a fully transient, Lagrangian CFD solver and so does not use a grid. Instead computations are done on SPH 'particles' that travel with the flow carrying local state information with them. Boundary geometries of almost arbitrary complexity may be included such as artery walls. Since the boundaries also contain SPH particles, it is possible to make these walls elastic and compliant with the fluid stresses exerted on the walls. The advantage of SPH is that no re-meshing of the domain is required to model the wall deformations. Furthermore SPH particles carry local state information and can thus track fluid history easily. This, combined with the ability to modify particles according to a rule base, means that we can grow thrombic protrusions into the flow and have them break off. We can then, in principle, follow this dangerous clot downstream into the cerebral vasculature. This is very hard in a traditional grid-based method and would enable investigation of critical medical problems well beyond the scope of traditional solvers. So the motivation for using SPH here, lies in the future deployment of the advantages described above.

The SPH methodology (Monaghan, 2012) consists of converting the partial differential equations encountered in fluid flow into algebraic equations. The interpolated value of a function A at any position \mathbf{r} can be expressed using SPH smoothing as:

$$A(\mathbf{r}) = \sum_b m_b \frac{A_b}{\rho_b} W(\mathbf{r} - \mathbf{r}_b, h) \quad (1)$$

where m_b and \mathbf{r}_b are the mass and density of particle b and the sum is over all particles b within a radius $2h$ of \mathbf{r} . Here $W(\mathbf{r}, h)$ is a C^2 spline based interpolation or smoothing kernel with radius $2h$ that approximates the shape of a Gaussian function. The gradient of the function A is given by differentiating the interpolation equation (1) to give:

$$\nabla A(\mathbf{r}) = \sum_b m_b \frac{A_b}{\rho_b} \nabla W(\mathbf{r} - \mathbf{r}_b, h) \quad (2)$$

Using these interpolation formulae and suitable Taylor series expansions for second order derivatives, one is able to convert parabolic partial differential equations into ordinary differential equations for the motion of the particles and the rates of change of their properties.

The SPH continuity equation is:

$$\frac{d\rho_a}{dt} = \sum_b m_b (\mathbf{v}_a - \mathbf{v}_b) \cdot \nabla W_{ab} \quad (3)$$

where ρ_a is the density of particle a with velocity \mathbf{v}_a and m_b is the mass of particle b . We denote the position vector from particle b to particle a by $\mathbf{r}_{ab} = \mathbf{r}_a - \mathbf{r}_b$ and let $W_{ab} = W(\mathbf{r}_{ab}, h)$ be the interpolation kernel with smoothing length h evaluated for the distance $|\mathbf{r}_{ab}|$. This form of the continuity equation is Galilean invariant (since the positions and velocities appear only as differences) and has good numerical conservation properties.

The momentum equation can be written as:

$$\frac{d\mathbf{v}_a}{dt} = \mathbf{g} - \sum_b m_b \left[\begin{array}{c} \left(\frac{P_b}{\rho_b^2} + \frac{P_a}{\rho_a^2} \right) \\ - \frac{\zeta}{\rho_a \rho_b (\mu_a + \mu_b)} \frac{\mathbf{v}_{ab} \mathbf{r}_{ab}}{\mathbf{r}_{ab}^2 + \eta^2} \end{array} \right] \nabla_a W_{ab} \quad (4)$$

where P_a and μ_a are pressure and fluid viscosity (0.0004 Pa.s) of particle a and $\mathbf{v}_{ab} = \mathbf{v}_a - \mathbf{v}_b$. Here ζ is a factor associated with the viscous term, η is a small parameter used to smooth out the singularity at $\mathbf{r}_{ab}=0$ and \mathbf{g} is the gravity vector. For more detail see Cleary et al. (2007).

The SPH method used here is quasi-compressible with the pressure given by an equation of state:

$$P = P_0 \left[\left(\frac{\rho}{\rho_0} \right)^\gamma - 1 \right] + P_b \quad (5)$$

where P_0 is the magnitude of the pressure, and ρ_0 is the reference density (1000 kg/m³). P_b is applied as a baseline pressure for the filled artery and was 1 kPa for this study. For blood we use $\gamma = 7$. This pressure is then used in the SPH momentum equation (3) to give the particle motion.

Carotid artery geometry

A real clinical patient geometry of a carotid bifurcation extracted from CT scan is shown in Figure 1. A surface mesh was created for this geometry and rigged to a virtual skeleton using the linear blend method (Kavan et al., 2008), using Autodesk Maya™ software (Autodesk Inc., San Rafael, CA, USA). Modification of this skeleton in

Maya then directly controls the deformation of the artery mesh. Finally, the mesh nodes are replaced with SPH boundary nodes for calculation of fluid-boundary forces in our simulations. The skeleton for the ICA branch is bent through an angle θ as shown in Figure 1. This defines a new ICA angle for each geometry variation.

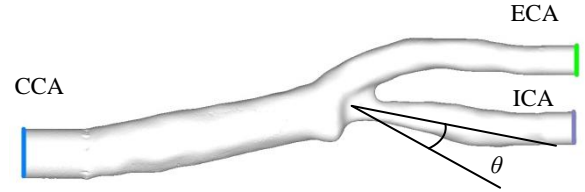


Figure 1: Geometry of carotid bifurcation showing the Common Carotid Artery (CCA) inflow and the Internal (ICA) and External (ECA) Carotid Artery outflows (coloured). Also shown is the ICA bending angle.

Pulsatile flow profile

Following each expulsion of blood from the heart and into the aorta, a pressure wave propagates downstream through the arterial system generating local changes in pressure. These transients can significantly alter the flow field through the arteries. It may also depend on wall elasticity and blood rheology, however these are often regarded as secondary effects relative to flow pulsatility. So here we assume that the boundaries are rigid and that blood behaves as a Newtonian fluid.

The physiological profile of a real pressure pulse at the entrance of the CCA depends on the cyclic pumping of the heart, the distensibility of the walls, and upstream and downstream pressures. During the diastolic phase of the heart cycle, when flow from the ventricle to the aorta is shut off, a non-zero flow through the arterial system is maintained as the elastic walls of the aorta contract.

The pulsatile flow profile was used previously in Sinnott et al. (2006). This is generated by a time-varying velocity boundary condition at the inflow. We approximate the physiological pulse as sinusoidal as shown in Figure 2. The period used was 0.5 s corresponding to a rapid heartbeat of 120 beats per minute (or 2 Hz). The duration of the pulse is much shorter (at 0.125 s). The maximum velocity is 0.5 m/s and the minimum is 0.1 m/s. A steady flow trailing the pulse represents the cut-off in supply from the heart during diastole. In a real pulse, there can be a degree of backflow during this time giving a small, negative pressure.

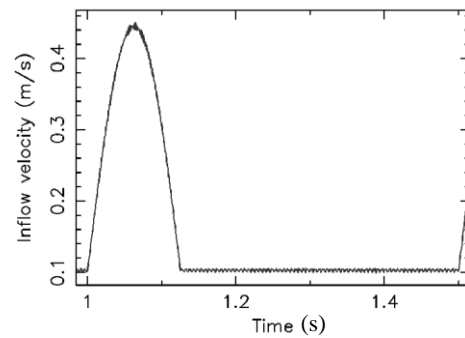


Figure 2: Pulsatile flow profile at the start of the common carotid artery. This is shown for a single pulse lasting 0.125 s and repeating every 0.5 s.

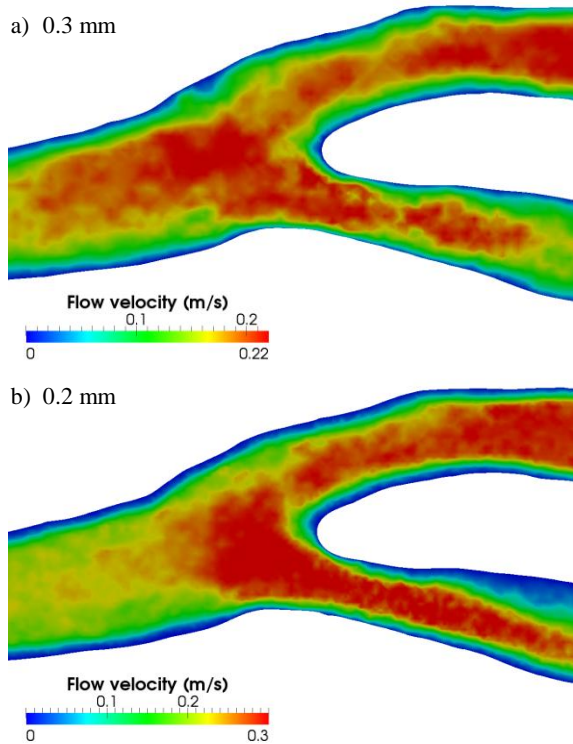


Figure 3: Comparison of the flow field through the base case artery at different flow resolutions, for an SPH particle separation of a) 0.3 mm and b) 0.2 mm.

RESOLUTION STUDY

We compare the flow field for an SPH particle separation of 0.2 mm and 0.3 mm to assess the effect of resolution on the flow predictions. Figure 3 shows the flow for the two resolutions at a time corresponding to when the wave reaches the bifurcation. The velocity distribution is qualitatively similar for the two cases, but the peak velocity through the lower branch (ICA) is 27% lower for the coarser 0.3 mm resolution case. This resolution corresponds to just 9 particles across the minimum ICA diameter of the stenosed (constricted) region immediately downstream of the bifurcation. For the 0.2 mm resolution, this is equivalent to 13.5 particles across. Since the velocity distribution (if not magnitude) appears independent of flow resolution we use the finer 0.2 mm SPH particle separation for the rest of the simulations in this paper.

FLOW FIELD FOR BASE CASE GEOMETRY

We now consider the time-varying nature of the flow field for the base case arterial geometry in more detail. Figure 4 shows the effect of the pulsatility of the flow on the instantaneous flow field inside the bifurcation. We compare the peak pulse and steady flow conditions in the artery. The pulse propagates as a pressure wave and its time of arrival at the bifurcation is delayed by 0.0025 s with respect to the profile at the CCA shown in Figure 2.

Figure 4a shows the velocity distribution just after the arrival of the peak of the pulse (1.1 s). They are elevated in both the upper and lower branches to about 0.35-0.4 m/s and are mostly constant along the length of the ECA branch due to the near constant diameter of the branch along its length. The high speed jet in the ICA branch

extends the full length of the branch. It is angled downward leading to a low flow region (< 0.05 m/s) near the top of the ICA branch.

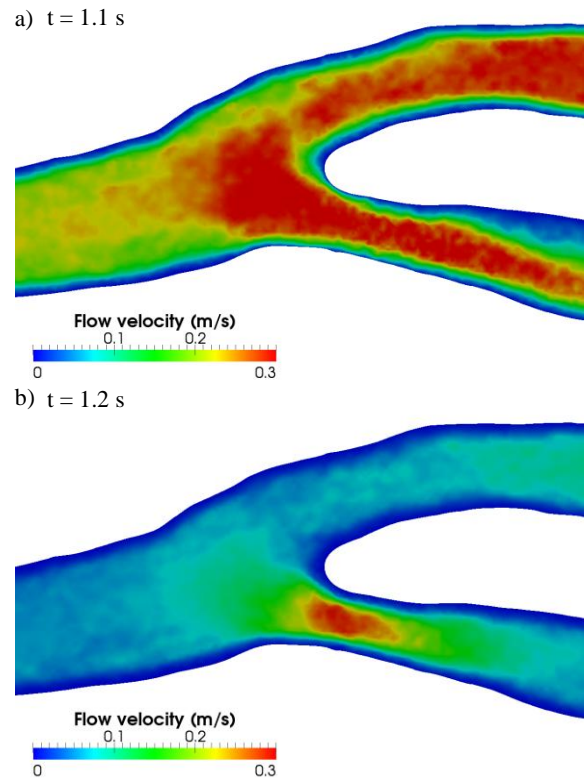


Figure 4: Flow through the base case carotid bifurcation during: a) the peak of the pulse; b) steady flow conditions after the pulse.

Following the trailing edge of the pulse, steady flow resumes (by 1.2 s). Figure 4b shows flow directed through both the ECA (upper) and ICA (lower) branches. However, the reduced diameter in the stenosed region of the ICA immediately after the junction constricts the flow resulting in a high speed jet (0.23-0.26 m/s). Steady flow at a reduced speed (~ 0.1 m/s) continues throughout the ECA branch. The high-speed flow is more localised to the stenosed region of the ICA (as in Figure 4a) but it is now more fully developed with a peak speed of 0.3 m/s in the centre of the jet.

COMPARISON OF FLOW AND WALL SHEAR STRESS FOR DIFFERENT ICA ANGLES

Next we explore the effect of changes in the amount of bending of the lower ICA branch. ICA angles of -16.5° (the maximum possible without resulting in self intersecting geometry) and 30° are considered. This gives a broad range ($\sim 45^\circ$) of ICA angle which is sufficient for assessing any effect that this critical angle may have on the flow. SPH flow simulations were run using the same inflow/outflow boundary conditions as used for the base case.

Figure 5 shows predictions of the flow (left) and the wall shear stress (WSS) (right) for each of the three ICA angle variants just after the arrival of the peak of the pressure pulse. The flow in general appears to be fairly insensitive to the change in ICA angle. The only significant change appears to be that as the angle increases the high speed jet (coloured red) through the stenosed region of the ICA

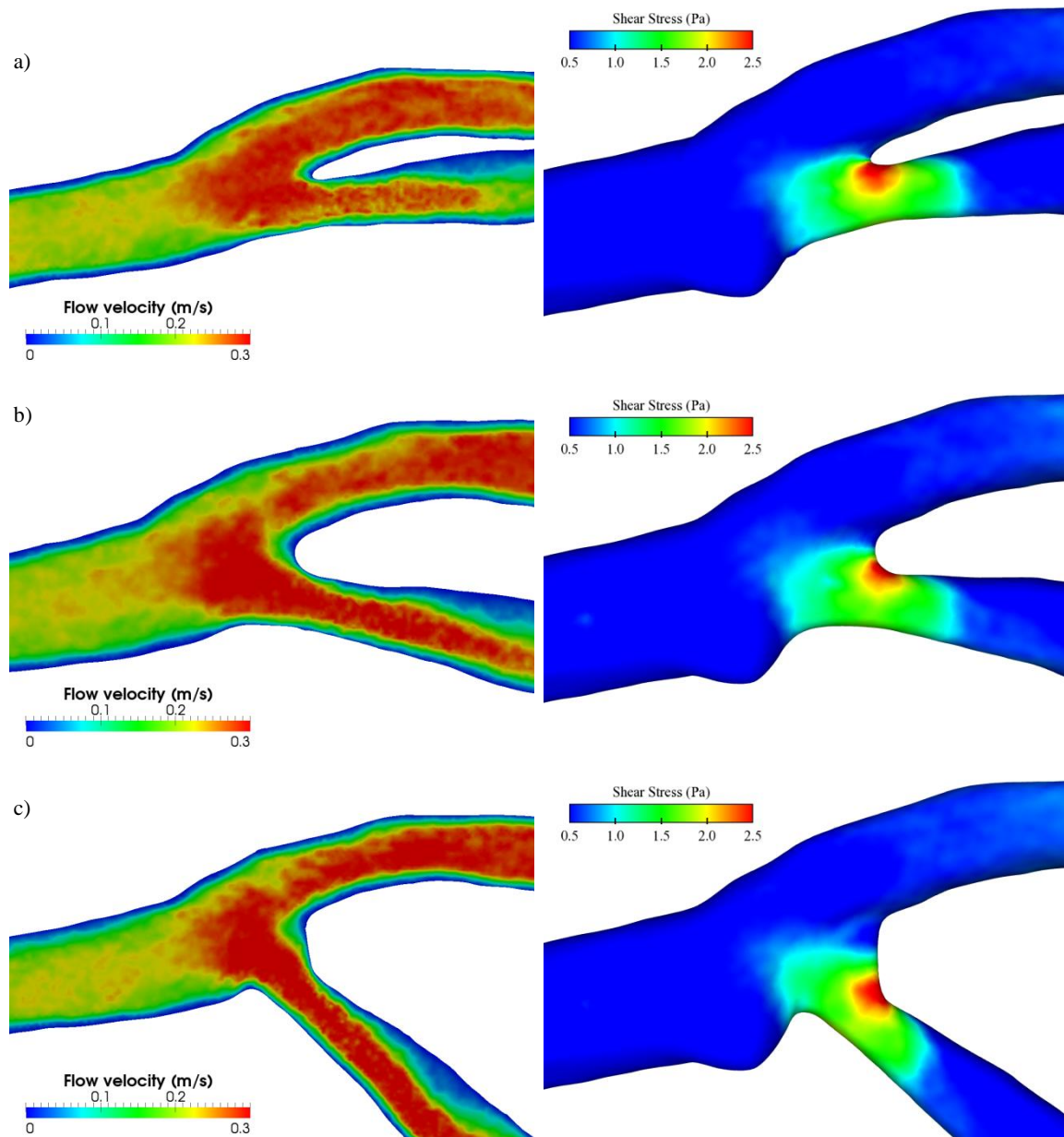


Figure 5: Comparison of cross-sectional flow (left) and 3D profiles of WSS predictions (right) for different ICA angle geometry with the ICA (lower branch) bent, relative to the base case geometry, by a) -16.5° ; b) 0° (base case); c) 30° .

extends further along the branch. This does not have any noticeable effect on the WSS on the artery wall and therefore the WSS also appears insensitive to ICA angle.

For the base case, moderately high WSS extends from just prior to the bifurcation and through the ICA to just downstream of the stenosed region. This is consistent with WSS distributions predicted by Morbiducci et al. (2012) who considered the effect of rheology on bulk flow (and WSS) in a carotid artery. The peak WSS occurs where there is a steep ramp up in flow speed for the high speed jet in the stenosis. In comparison, the WSS in the ECA branch is negligible. That a simple geometric change does not significantly alter the flow is not a completely unexpected result since the same inflow/outflow boundary conditions are used for each case. Therefore the pressure drop (and corresponding flow rate) across each branch is very similar. In the full arterial network, the real pressures occurring at our outflow positions will be influenced by

the branching, curvature and narrowing of the network downstream. To accurately model the local flow through short arterial sections requires clinical measurement of the real inflow and outflow pressures (or flow velocities). Alternatively, in the absence of such measurements it will be necessary to couple models of flow in these arterial sections to larger-scale network models of the full circulation. For more discussion of 1D/3D hybrid models, the reader is referred to Johnson et al. (2011) and Anor et al. (2010).

EFFECT OF ICA OUTFLOW PRESSURES

To understand the effect of different outflow conditions on the flow field and WSS distribution we vary the outflow pressure of the ICA for the base case geometry. Figure 6 shows the flow coloured by velocity (left) and the artery wall coloured by WSS (right). The time shown corresponds to just after the peak of the pulse arrives at the

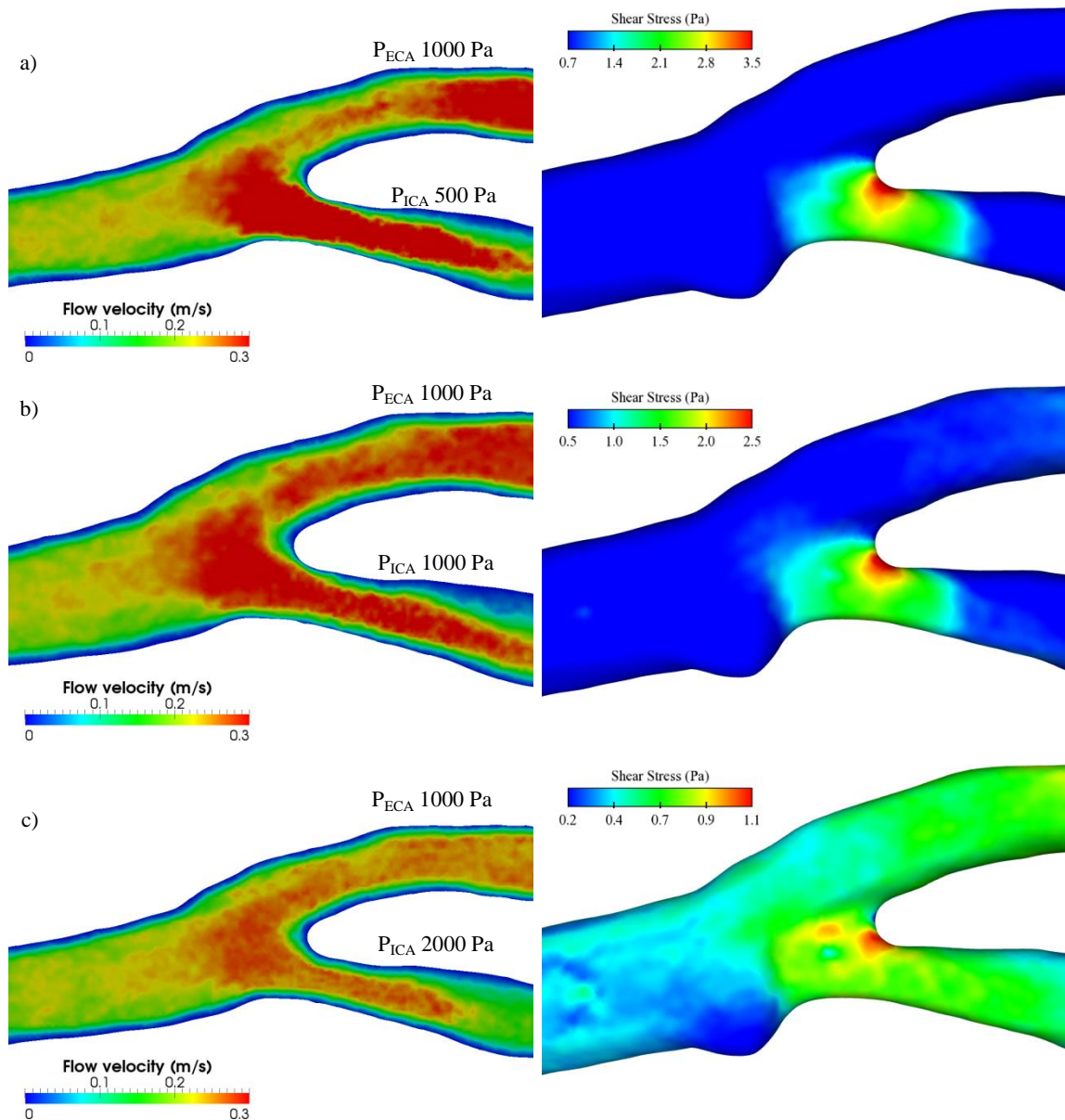


Figure 6: Comparison of flow (left) and WSS predictions (right) for different outflow pressure conditions for the ICA of: a) 500 Pa; b) 1000 Pa (base case); c) 2000 Pa. The outflow pressure for the ECA (upper branch) is 1000 Pa for each simulation.

bifurcation. Figure 6b shows the flow and WSS for the base case. Figure 6a shows the case where the outflow pressure for the ICA branch is halved while the pressure at the end of the ECA remains the same as for the base case (1 kPa). This means that there is less relative resistance to flow through the ICA than through the ECA. There is only a very mild reduction in the flow velocities in the ECA.

The angle of the high-speed jet through the ICA stenosis is directed slightly upward relative to that of the base case and there is a mild increase in peak (red) velocities at the start of the ICA. The distribution of WSS is very similar to the base case but the peak WSS is 40% higher due to the steeper velocity gradient near the upper wall of the ICA.

Figure 6c shows the case with double the outflow pressure at the end of the ICA. The peak velocities in both branches are reduced and the high speed jet extends a much shorter distance through the ICA than for the base case. The peak

stress in the ICA is greatly reduced by 66% and is comparable to the low levels of WSS existing along both branches.

Figure 7 shows the history of the volumetric flow rates exiting the ECA and ICA branches for each of these three cases. Figure 7a shows that when the ICA outflow pressure is halved, the peak flow rate corresponding to the arrival of the pulse is roughly the same for both branches. This is shown clearly in Figure 6a. This is because the ICA stenosis provides substantial resistance that restricts the peak flow rate through the ICA. The arrival of the high speed pulse elevates pressures inside the stenosis so that they exceed the outflow pressure in the ECA redirecting more flow through the ECA. In contrast, the steady flow during diastole is almost zero through the ECA so that almost all flow is directed out through the ICA. Figure 7b shows the base case where the outflow pressures for the ICA and ECA are equal. The volumetric flow through

both branches is similar during both systole and diastole. Figure 7c shows the case where the ICA outflow pressure is doubled. During systole, the flow rate through the ICA is 70% that of the flow through the ECA. However during diastole there is almost zero flow out of the ICA, so that almost all of the flow now exits through the ECA branch.

From this we can see that there is a complex relationship between time-varying flow, regions of flow constriction and the downstream pressure conditions. During diastole the flow rates through each of the branches appear well defined by the applied outflow conditions. However, the arrival of the pulse at the bifurcation leads to a ramp up in pressures in the stenosed region such that flow is then preferentially directed into the ECA. This suggests that time-varying flow and steady flow may be controlled differently by stenosed regions. This will be further complicated by the wall compliance which will tend to stretch elastic regions in order to relieve the pressure. This may lead to large strain at the interface between elastic tissue and rigid plaques which may influence changes in plaque morphology. This in turn may enhance the risk of rupture/clotting leading to stroke conditions.

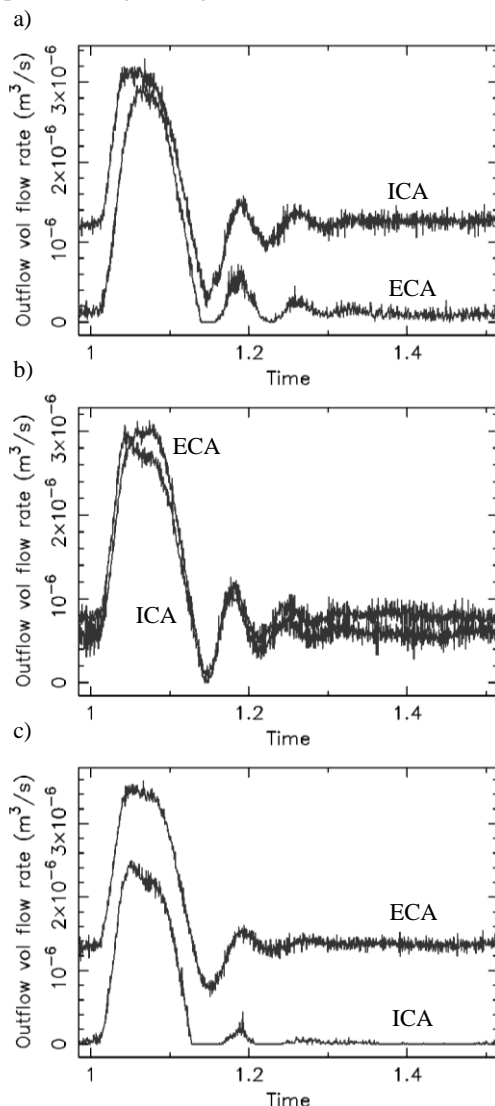


Figure 7: Effect of outflow pressure boundary conditions at the end of the ICA branch on outflow volumetric flow rates for: a) 500 Pa; 1000 Pa; 2000 Pa. The outflow pressure for the ECA branch is kept constant at 1 kPa.

CONCLUSION

We have investigated the effect of ICA angle and outflow boundary conditions on the flow and WSS in a real carotid bifurcation. For the same outflow conditions on ICA and ECA, varying the ICA angle from -16.5° to 30° (relative to the base case angle of 35°) showed almost no change in flow field or in the predicted WSS. This appears to be a consequence of having the same pressure drop across each branch for each case.

Increasing the ICA outflow pressure redirects more flow to the ECA and results in a drop in the peak WSS at the bifurcation. There is a complex relationship between time-varying flow, outflow boundary conditions and constricted regions of geometry. During systole when the flow rate rapidly increases, rising pressures in stenosed regions can lead to significant flow bottlenecks which control how flow is channelled through a bifurcation.

REFERENCES

- PHAN T.G., BEARE R.J., JOLLEY D, DAS G, REN M, WONG K, CHONG W, SINNOTT M.D., HILTON J.E. and SRIKANTH V., (2012), "Carotid artery anatomy and geometry as risk factors for carotid atherosclerotic disease", *Stroke*, **43**(6), 1596-601.
- NGUYEN K.T., CLARK C.D., CHANCELLOR T.J. and PAPAVALASSILOU D.V., (2008), "Carotid geometry effects on blood flow and on risk for vascular disease", *J.Biomech* **41**, 11-19.
- CLEARY, P., PRAKASH, M., HA, J., STOKES, N. and SCOTT, C. (2007), "Smooth particle hydrodynamics: status and future potential", *Prog. In CFD*, **7**, 70-90.
- MONAGHAN, J.J., (2012), "Smoothed Particle Hydrodynamics and Its Diverse Applications", *Annual Review of Fluid Mechanics*, **44**, 323-346.
- KAVAN, L., COLLINS, S., ZARA, J. and O'SULLIVAN, C., (2008), "Geometric Skinning with Approximate Dual Quaternion Blending", *ACM T Graphic*, **27**(4), Article 105, pp. 1-23.
- SINNOTT M., CLEARY, P.W. and PRAKASH, M., (2006), "An investigation of pulsatile blood flow in a bifurcation artery using a grid-free method", *Proc: 5th Int Conf on CFD in the Process Industries*, ID: 119Sin.
- MORBIDUCCI, U., GALLO, D., MASSAI, D., PONZINI, R., DERIU, M.A., ANTIGA, L., REDAELLI, A. and MONTEVECCHI, F.M. (2012), "On the importance of blood rheology for bulk flow in hemodynamic models of the carotid bifurcation", *J. Biomech.*, **44**, 2427-2438.
- JOHNSON, D.A., NAIK, U.P. and BERIS, A.N., (2011), "Efficient implementation of the proper outlet flow conditions in blood flow simulations through asymmetric arterial bifurcations", *Int. J. Numer. Meth. Fluids*, **66**, 1383-1408.
- ANOR, T., GRINBERG, L., HYOUNGSU, B., MADSEN, J.R., JAYARAMAN, M.V. and KARNIADAKIS, G.E., (2010), "Modeling of blood flow in arterial trees", *Wiley Interdisciplinary Reviews: Systems Biology and Medicine*, **2**(5), 612-623.